INTERNATIONAL JOURNAL FOR NUMERICAL METHODS IN FLUIDS
Int. J. Numer. Meth. Fluids 2003; **41**:185–208 (DOI: 10.1002/fld.434)

Dynamic analysis of baffled fuel-storage tanks using the ALE finite element method

J. R. Cho*,†,‡ and S. Y. Lee

School of Mechanical Engineering, Pusan National University, Kumjung-Ku, Pusan 609-735, Korea

SUMMARY

This paper is concerned with the parametric investigation on the structural dynamic response of moving fuel-storage tanks with baffles. Since the structural dynamic behaviour is strongly coupled with interior liquid motion, the design of a fuel-storage tank securing the structural stability becomes the appropriate suppression of the flow motion, which is in turn related to the baffle design. In order to numerically investigate the parametric dynamic characteristics of moving tanks, we employ the arbitrary Lagrangian–Eulerian (ALE) finite element method that is widely being used to deal with the problems with free surface, moving boundary, large deformation and interface contact. Following the theoretical and numerical formulations of fluid-structure interaction problems, we present parametric numerical results of a cylindrical fuel-storage tank moving with uniform vertical acceleration, with respect to the baffle number and location, and the inner-hole diameter. Copyright © 2003 John Wiley & Sons, Ltd.

KEY WORDS: baffled fuel-storage tank; ALE finite element method; fractional step method; remeshing and smoothing; unsteady dynamic response; baffle parameter

1. INTRODUCTION

In either stationary or moving liquid-storage tanks, the structural dynamic response is greatly influenced by interior liquid motion. Needless to say, it is because two distinguished dynamic modes, the structure deformation and the liquid sloshing motion exhibit a strong dynamic coupling in such interaction systems [1]. Therefore, the elaborate dynamic analysis considering the complete coupling between two dynamic media as well as the mechanical device [2, 3] for suppressing (or controlling) liquid motion becomes essential for the design of liquid-storage tanks securing the structural stability and the maneuverability.

According to our literature survey, the structural dynamic analysis of moving liquid-storage tanks was initiated by Housner [4], Abramson [5], Bauer [6] and other early investiga-

* Correspondence to: J. R. Cho, School of Mechanical Engineering, Pusan National University, Kumjung-Ku, Pusan 609-735, Korea.
† E-mail: jrcho@hyowon.pusan.ac.kr
‡ Associate Professor.

Contract/grant sponsor: Agency for Defense Development; contract/grant number: ADD-00-5-6

Received August 2001
Revised 15 July 2002

tors, targeting for the aerospace engineering application. But, which was quite simplified and restricted. After that, the analysis and design technologies have been continuously and considerably advanced thanks to the intensive works by numerous subsequent investigators.

As is well classified in a paper by Welt and Modi [3], a number of passive devices for suppressing liquid motion in fluid-structure interaction systems have been introduced. Among them, the classical baffle which partitions a tank into several partially separated regions are widely being adopted for general engineering fuel-storage tanks. Needless to say, the reason is because it is more practical and easy to install within the tank structure. By the way, several design parameters such as the baffle number, the arrangement type and baffle spacing, the inner hole size allowing fuel to flow are directly associated with the baffle design, from the aspect of structural, flow and maneuvering stabilities [7, 8].

On the other hand, the realistic numerical analysis of such dynamic characteristics requires the complete coupling, between the structure deformation and the liquid motion, and the reliable technique for remeshing the extremely distorted elements. For this purpose, the arbitrary Lagrangian–Eulerian (ALE) approach is now being employed widely in fluid-structure interaction problems. Until such an effective numerical analysis method has become pervasive, most studies on the structural dynamic analysis of baffled liquid-storage tanks had relied on the theoretical and experimental methods as well as the separate numerical analysis by mass-adding technique [9, 10]. As a result, early numerical studies on the dynamic response expectation were not fully comprehensive.

The LAE concept was introduced originally by Hirt *et al*. [11] for the finite difference scheme, later it has been extended to the finite element method by numerous computational specialists, such as References [12–14]. As is well described in references, this approach is based on the arbitrary movement of a reference domain (or the mesh movement), as a third co-ordinate additional to the common material and spatial co-ordinates. With the introduction of this reference co-ordinate, together with a good remeshing algorithm, the flow movement can be successfully simulated.

In this paper, we intend to numerically examine the effects of disc-type elastic baffle on the dynamic characteristics of cylindrical fuel-storage tank boosting with uniform vertical acceleration, as a first step for the concrete parametric understanding of the above-mentioned dynamic characteristics. For this goal, we use the finite element method for the structural motion and the interior fuel flow, while incorporating with the ALE kinematic description, by assuming interior fuel flow to be incompressible. By varying the baffle number, the baffle distance from the fuel free surface and the inner-hole diameter, we parametrically investigate the time-history response of the deformation and the effective stress of baffle and cylindrical container and hydrodynamic pressure distributions.

This paper is organized as follows. The theoretical formulation on the incompressible viscous fluid-structure interaction, together with the ALE kinematic description, is given in Section 2. We next describe the numerical approximations of completely coupled fluid-structure interactions in the ALE kinematic description and the remeshing scheme in Section 3. After that, we present and discuss the numerical results in Section 4 according to parametric dynamic experiments. Finally, we make the concluding remarks in Section 5.

2. INCOMPRESSIBLE VISCOUS FLUID-STRUCTURE INTERACTION

2.1. Problem description

Figure 1 shows a cylindrical tank of uniform thickness t, with a metal baffle of thickness t_B and inner-hole diameter D_B, in which incompressible viscous fuel is filled up to the height H_F. Throughout this paper, subscripts F and B refer to the parameters of fuel and baffle, respectively. As mentioned before, the structural dynamic response of storage tanks is characterized by the number and location of baffles, the inner-hole diameter, the baffle spacing, the baffle thickness, and so on.

In the Cartesian co-ordinate system, the structural dynamic motion of the tank structure occupying the spatial domain Ω is governed by

$$\sigma_{ij}(\mathbf{u})_{,j} - c\frac{\partial u_i}{\partial t} = \rho\left(\frac{\partial^2 u_i}{\partial t^2} - g_i\right) \quad \text{in } \Omega \times (0,T] \tag{1}$$

with initial and boundary conditions:

$$u_i(0) = \dot{u}_i(0) = 0 \quad \text{in } \Omega \tag{2}$$

$$u_i = \hat{u}_i \quad \text{on } \partial\Omega_D \times (0,T] \tag{3a}$$

$$\sigma_{ij}n_j = t_i \quad \text{on } \partial\Omega_I \times (0,T] \tag{3b}$$

In which, c, ρ and g_i indicate, respectively, the damping coefficient, the structure density and gravity acceleration components, $\partial\Omega_D$ the displacement boundary region, and $\partial\Omega_I$ the common fuel-structure interface. In most cases, the surface traction is given by $t_i n_i = -p$, when denoting p be the hydrodynamic pressure of fuel. On the other hand, external loading is usually of acceleration-type excitation.

The time-dependent unsteady-state viscous flow of interior incompressible fuel occupying the time-varying spatial domain $\Omega_F(t)$ is characterized by the mass and momentum conservation laws such that

$$v_{i,i} = 0 \quad \text{in } \Omega_F \times (0,T] \tag{4}$$

$$\frac{\partial v_i}{\partial t} + v_j v_{i,j} - \frac{1}{\rho_F}\tau_{ij,j} = g_i \quad \text{in } \Omega_F \times (0,T] \tag{5}$$

where v_i and ρ_F indicate the flow velocity components and the fuel density, respectively. By denoting the kinematic viscosity of fuel by μ, the stress tensor τ_{ij} is constituted as follows:

$$\tau_{ij} = \mu(v_{i,j} + v_{j,i}) - p\delta_{ij} \tag{6}$$

The time-varying boundary $\partial\Omega_F(t)$ of the fuel domain is composed of the free surface $\partial\Omega_F^S$ and the fuel-structure interface $\partial\Omega_I$ such that $\partial\Omega_F = \overline{\partial\Omega_F^S \cup \partial\Omega_I}$. Then, the momentum equation (5) is to be solved with the initial condition

$$v_i(\mathbf{x},0) = 0 \quad \text{in } \Omega_F \tag{7}$$

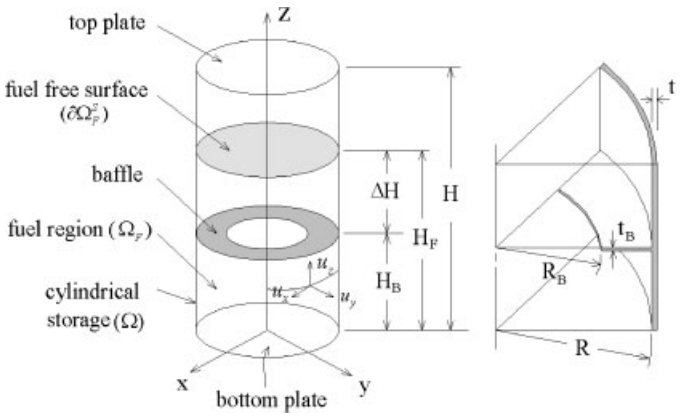

Figure 1. Definition of geometry and symbols of cylindrical fuel-storage tank with a baffle.

and the boundary conditions given by

$$v_i = \frac{\partial u_i}{\partial t} \quad \text{on } \partial\Omega_1 \times (0, T] \tag{8a}$$

$$\tau_{ij} n_j = \hat{t}_i \quad \text{on } \partial\Omega_F^S \times (0, T] \tag{8b}$$

where $\hat{t}_i$ are the traction components acting on the fuel free surface. The velocity boundary condition (8a) indicates no slip and no penetration, but the former disappears when the flow is assumed to be inviscid.

2.2. *ALE kinematic description*

The numerical approach for the initial–boundary value problems with significant time-varying domain and boundary, such as free surface flows, fluid-structure interactions, large deformation problems and moving boundary problems, has been a great challenging subject in computational mechanics. As is well known, there exist three basic approaches in the numerical implementation of such problems, Lagrangian, Eulerian and ALE methods.

In the Lagrangian numerical approach, the time-varying boundary moves exactly with the material particle velocity so that the boundary is accurately updated. However, such boundary movement may frequently make an entire mesh distorted excessively. As a result, a successful and efficient numerical accomplishment requires successive remeshing of mesh, until the final time stage. On the other hand, a mesh domain in the Eulerian method is spatially fixed and set to be larger than the actual material domain. And, the moving boundary should be identified locally by any suitable characteristic function, such as the material volume fraction function characterizing the material and void regions. However, one should refine the mesh locally in order to accurately identify the boundary interface.

In the ALE method which has been introduced to invoke only the computational merits of the previous two methods, the mesh domain is identical to the material domain such that its boundary tracks the material velocity while keeping the entire mesh fairly regular [11–13]. As

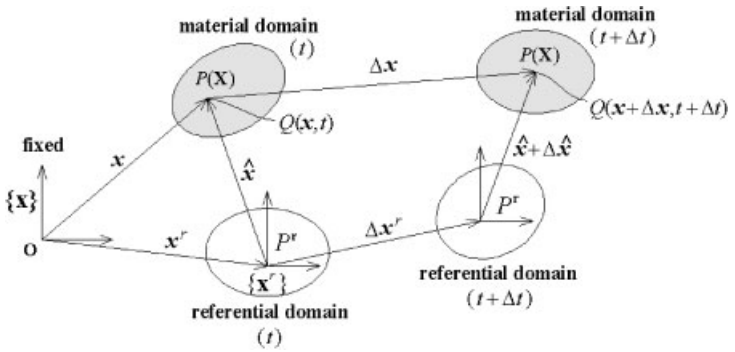

Figure 2. Representation of material, spatial and reference domains.

is well known, in the ALE formulations the Lagragian (or material) and Eulerian (or spatial) domains and an arbitrary referential domain are employed. As usual, the referential domain is defined by the computational mesh (or grid) domain.

Referring to Figure 2, we consider a material domain and a referential one at time t, where any material particle moving with the velocity $\mathbf{v}$ is denoted by P. Next, we introduce a fixed Cartesian co-ordinate system $\{X\}$ with unit vectors $\mathbf{e}_i$, then the material particle P is identified by the Lagrangian co-ordinate $\mathbf{X}$. In addition, we assume that the point P^{r} positioned at $\mathbf{x}^{\mathrm{r}}$ in the referential domain at time t moves with an arbitrary velocity $\hat{\mathbf{v}}$, to which we attach another moving Cartesian co-ordinate system $\{X^{\mathrm{r}}\}$ with unit vectors $\hat{\mathbf{e}}_i$. Then, the spatial position of the same material particle P at time t can be expressed as follows: either $\mathbf{x} = x_i \mathbf{e}_i$ in the former co-ordinate system or $\hat{\mathbf{x}} = \hat{x}_i \hat{\mathbf{e}}_i$ in the latter one.

Let us assume that the material particle P and the referential co-ordinate system $\{X^{\mathrm{r}}\}$ move to the new positions $\mathbf{x} + \Delta\mathbf{x}$ and $\mathbf{x}^{\mathrm{r}} + \Delta\mathbf{x}^{\mathrm{r}}$, respectively, with the absolute velocities $\mathbf{v}$ and $\hat{\mathbf{v}}$ during Δt. Then, the following relations hold:

$$\hat{\mathbf{x}} = \mathbf{x} - \mathbf{x}^{\mathrm{r}} \tag{9a}$$

$$\hat{\mathbf{x}} + \Delta\hat{\mathbf{x}} = (\mathbf{x} + \Delta\mathbf{x}) - (\mathbf{x}^{\mathrm{r}} + \Delta\mathbf{x}^{\mathrm{r}}) \tag{9b}$$

Reminding $\Delta\mathbf{x} = \mathbf{v}\Delta t$ and $\Delta\mathbf{x}^{\mathrm{r}} = \hat{\mathbf{v}}\Delta t$, we have

$$\Delta\hat{\mathbf{x}} = (\mathbf{v} - \hat{\mathbf{v}})\Delta t \tag{10}$$

Now, let us denote $Q(\mathbf{x}, t)$ be a flow quantity associated with the position $\mathbf{x}$ at time t, then it can be mapped into the $\{X^{\mathrm{r}}\}$ co-ordinate system: $Q(\mathbf{x}, t) = Q\{\mathbf{x}(\hat{\mathbf{x}}), t\} = \hat{Q}(\hat{\mathbf{x}}, t)$, according to the co-ordinate transformation (9a). The moving material particle situated there will assume for the value $Q(\mathbf{x}, t)$ at time t and $Q(\mathbf{x} + \Delta\mathbf{x}, t + \Delta t)$ at the new position $\mathbf{x} + \Delta\mathbf{x}$ in a short time interval Δt along the flow path.

Then the material (or substantial) derivative $\mathrm{D}Q/\mathrm{D}t$ of the quantity Q following the material particle P, with respect to the referential co-ordinate system $\{X^{\mathrm{r}}\}$, is defined as follows:

$$\left.\frac{\mathrm{D}Q}{\mathrm{D}t}\right|_{(X,t)} = \lim_{\Delta t \to 0} \frac{\hat{Q}(\hat{\mathbf{x}} + \Delta\hat{\mathbf{x}}, t + \Delta t) - \hat{Q}(\hat{\mathbf{x}}, t)}{\Delta t} \tag{11}$$

According to the Taylor series expansion for two-variable functions, we have

$$\hat{Q}(\hat{\mathbf{x}}+\Delta\hat{\mathbf{x}},t+\Delta t)=\hat{Q}(\hat{\mathbf{x}},t)+\left.\frac{\partial\hat{Q}}{\partial t}\right|_{(\hat{\mathbf{x}},t)}\cdot(\Delta t)+\left.\frac{\partial^2\hat{Q}}{\partial t^2}\right|_{(\hat{\mathbf{x}},t)}\cdot(\Delta t)^2+\cdots + \left.\frac{\partial\hat{Q}}{\partial\hat{\mathbf{x}}}\right|_{(\hat{\mathbf{x}},t)}\cdot(\Delta\hat{\mathbf{x}})+\left.\frac{\partial^2\hat{Q}}{\partial\hat{\mathbf{x}}^2}\right|_{(\hat{\mathbf{x}},t)}\cdot(\Delta\hat{\mathbf{x}})^2+\cdots \tag{12}$$

where the multi-index notation [14] is used for expressing the spatial derivatives of multi-variable functions. Substituting relation (12) into Equation (11) leads to

$$\left.\frac{\mathrm{D}Q}{\mathrm{D}t}\right|_{(\mathbf{X},t)}=\left.\frac{\partial\hat{Q}}{\partial t}\right|_{(\hat{\mathbf{x}},t)}+\mathbf{s}\cdot\left.\frac{\partial\hat{Q}}{\partial\hat{\mathbf{x}}}\right|_{(\hat{\mathbf{x}},t)}=\left.\frac{\partial Q}{\partial t}\right|_{(\mathbf{x},t)}+\mathbf{s}\cdot\left.\frac{\partial Q}{\partial\mathbf{x}}\frac{\partial\mathbf{x}}{\partial\hat{\mathbf{x}}}\right|_{(\mathbf{x},t)} \tag{13}$$

where $\mathbf{s}=(\mathbf{v}-\hat{\mathbf{v}})$ is defined as the relative (or convective) velocity between the material and referential velocities.

By comparing Equation (13) with the standard Eulerian description, one can find that the only difference is the convective derivative, the last term in the right-hand side. Hence, the previous Navier–Stokes equations in the ALE description are written as follows:

$$v_{i,i}=0 \quad \text{in } \Omega_{\mathrm{F}}\times(0,T] \tag{14a}$$

$$\frac{\partial v_i}{\partial t}+(v_j-\hat{v}_j)v_{i,j}-\frac{1}{\rho_{\mathrm{F}}}\tau_{ij,j}=g_i \quad \text{in } \Omega_{\mathrm{F}}\times(0,T] \tag{14b}$$

with no modification in the constitutive relation (6) and initial and boundary conditions (7)–(8).

From the relationship between the material and referential derivatives, we recognize that the ALE description can be switched to either the Lagrangian one by moving $\{X^{\mathrm{r}}\}$ with the material velocity (i.e. $\hat{\mathbf{v}}=\mathbf{v}$) or the Eulerian one by fixing $\{X^{\mathrm{r}}\}$ in space (i.e. $\hat{\mathbf{v}}=0$). In reality, the motion of referential domain is totally arbitrary in space and time, depending on the numerical simulation situation [15]. This implies that three description approaches can be effectively combined within single numerical analysis, according to the appropriate control of the mesh movement.

3. NUMERICAL FORMULATIONS

3.1. Finite element approximations

According to the principle of virtual work, we can obtain the weak form of Equation (1), to which we introduce the isoparametric finite element approximation to the dynamic displacement $\mathbf{u}(\mathbf{x},t)$:

$$\mathbf{u}(\mathbf{x},t)=\Phi(\mathbf{x})\cdot\bar{\mathbf{u}}(t) \tag{15}$$

with denoting Φ be the $(3 \times 3N)$ matrix composed of N basis functions. Then, we arrive at the usual numerical system of equations given by

$$\mathbf{M}\ddot{\bar{\mathbf{u}}} + \mathbf{C}\dot{\bar{\mathbf{u}}} + \mathbf{K}\bar{\mathbf{u}} = \mathbf{f} \tag{16}$$

in which the load vector $\mathbf{f}$ is due to the body force and the hydrodynamic pressure.

Next, we temporally discretize Equation (16) according to the Newmark constant-averaged-acceleration method [16]:

$$\mathbf{M}\ddot{\bar{\mathbf{u}}}^{n+1} + \mathbf{C}\dot{\bar{\mathbf{u}}}^{n+1} + \mathbf{K}\bar{\mathbf{u}}^{n+1} = \mathbf{f}^{n+1} \tag{17}$$

with

$$\dot{\bar{\mathbf{u}}}^{n+1} = \dot{\bar{\mathbf{u}}}^{n} + \Delta t(\ddot{\bar{\mathbf{u}}}^{n+1} + \ddot{\bar{\mathbf{u}}}^{n})/2 \tag{18a}$$

$$\bar{\mathbf{u}}^{n+1} = \bar{\mathbf{u}}^{n} + \Delta t \cdot \dot{\bar{\mathbf{u}}}^{n} + (\Delta t)^2[(\tfrac{1}{2} - \beta)\ddot{\bar{\mathbf{u}}}^{n} + \beta\ddot{\bar{\mathbf{u}}}^{n+1}] \tag{18b}$$

where the parameter β is 0.25 [16]. Substituting Equations (18a) and (18b) into Equation (17) leads to

$$\left[\mathbf{M} + \frac{\Delta t}{2}\mathbf{C} + \beta(\Delta t)^2\mathbf{K}\right]\ddot{\bar{\mathbf{u}}}^{n+1} = -\left[\frac{\Delta t}{2}\mathbf{C} + \left(\frac{1}{2} - \beta\right)(\Delta t)^2\mathbf{K}\right]\ddot{\bar{\mathbf{u}}}^{n} - [\mathbf{C} + \Delta t \cdot \mathbf{K}]\dot{\bar{\mathbf{u}}}^{n} - \mathbf{K}\,\bar{\mathbf{u}}^{n} + \mathbf{f}^{n+1} \tag{19}$$

We note here that the load vector $\mathbf{f}^{n+1}$ at time step $(n+1)$ is computed through

$$\mathbf{f}^{n+1} = \mathbf{f}^{n} + \int_{\partial\Omega_1} \Phi^{\mathrm{T}}(\mathbf{p}^{n} - \mathbf{p}^{n-1})\,\mathrm{d}s \tag{20}$$

where $\mathbf{p}$ indicates the time-step-wise finite element approximation of the hydrodynamic pressure field obtained from the Navier–Stokes system of Equations (14a) and (14b).

According to the Crank–Nicolson scheme, together with the arbitrariness of mesh velocity, the Navier–Stokes equations (14a) and (14b) in the ALE description can be temporally discretized as follows:

$$\frac{v_i^{n+1} - v_i^{n}}{\Delta t} + (v_j^{*} - \hat{v}_j^{n})v_{i,j}^{n+1/2} - \frac{1}{\rho_{\mathrm{F}}}\tau_{ij,j}^{n+1/2} = g_i \tag{21}$$

$$v_{i,i}^{n+1} = 0 \tag{22}$$

with

$$\tau_{ij,j}^{n+1/2} = \mu v_{i,jj}^{n+1/2} - p_{,i}^{n+1/2} \tag{23a}$$

$$v_i^{*} = v_i^{n+1/2} = (3v_i^{n} - v_i^{n-1})/2 \tag{23b}$$

In order to effectively solve the time-step-wise pressures and velocities satisfying the continuity constraint (22) accurately, we adopt here the *C*—fractional method proposed by Hayashi *et al.* [17]. In the conventional fractional methods stemmed from one by Chorin [18], the pressure gradient term in Equation (21) is decoupled from the convection, diffusion and external loading terms, according to the introduction of an intermediate velocity that does not satisfy the continuity constraint. Hence, at the next step, it should be corrected by the pressure obtained from the continuity equation. Even though this correction procedure could be improved by the well-known Chorin-type SIMPLE algorithm [19], it takes more numerical iterations for the converged velocity than the standard fractional step method.

Using the basic relation in the time-step scheme and Equation (21), together with relation (23a), we can rewrite the convection term such that

$$\begin{aligned}(v_j^* - \hat{v}_j^n)v_{i,j}^{n+1/2} &= (v_j^* - \hat{v}_j^n)\left[v_{i,j}^n + (v_i^{n+1} - v_i^n)_{,j}/2\right] \\ &= (v_j^* - \hat{v}_j^n)v_{i,j}^n - \frac{\Delta t}{2}(v_j^* - \hat{v}_j^n)\left[(v_k^* - \hat{v}_k^n)v_{i,k}^{n+1/2} + \frac{1}{\rho_F}\, p_{,i}^{n+1/2} - \frac{1}{\rho_F}\,\mu v_{i,kk}^{n+1/2} - g_i\right]_{,j} \\ &= (v_j^* - \hat{v}_j^n)v_{i,j}^n - \frac{\Delta t}{2}(v_j^* - \hat{v}_j^n)\Lambda_{i,j}^{n+1/2} \end{aligned} \tag{24}$$

where $\Lambda_i^{n+1/2}$ refers to the term $[\cdot]$. Substituting the above relation into Equation (21) leads to the time-step-wise velocity equations:

$$\frac{v_i^{n+1} - v_i^n}{\Delta t} + (v_j^* - \hat{v}_j^n)v_{i,j}^n + \frac{1}{\rho_F}\, p_{,i}^{n+1/2} - \frac{\mu}{\rho_F}\, v_{i,jj}^{n+1/2} - \frac{\Delta t}{2}(v_j^* - \hat{v}_j^n)\Lambda_{i,j}^{n+1/2} = g_i \tag{25}$$

with the initial condition (7) and

$$v_i^{n+1/2} = \partial u_i^{n+1/2}/\partial t \quad \text{on } \partial\Omega_I \tag{26a}$$

$$\tau_{ij}^{n+1/2} n_j = \hat{t}_i^{n+1/2} \quad \text{on } \partial\Omega_F^S \tag{26b}$$

Next, we take divergence to Equation (21) and enforce the continuity constraint (22). Then we can obtain the time-step-wise pressure equation from

$$\frac{1}{\rho_F}\, p_{,ii}^{n+1/2} = \frac{1}{\Delta t}\, v_{i,i}^n - \left[(v_j^* - \hat{v}_j^n)v_{i,j}^{n+1/2} - \frac{\mu}{\rho_F}\, v_{i,jj}^{n+1/2} - g_i\right]_{,i} \tag{27}$$

with the initial condition (7) and the pressure boundary conditions given by

$$p^{n+1/2} = 0 \quad \text{on } \partial\Omega_F^S \tag{28a}$$

$$p_{,i}^{n+1/2} n_i = -\frac{\rho_F}{\Delta t}(\partial u_i^{n+1}/\partial t - \partial u_i^n/\partial t)n_i = \gamma^{n+1/2} \quad \text{on } \partial\Omega_I \tag{28b}$$

The variational forms corresponding to the above two semi-discretized equations (25) and (27) could be obtained by introducing the virtual velocity and pressure, respectively (see the

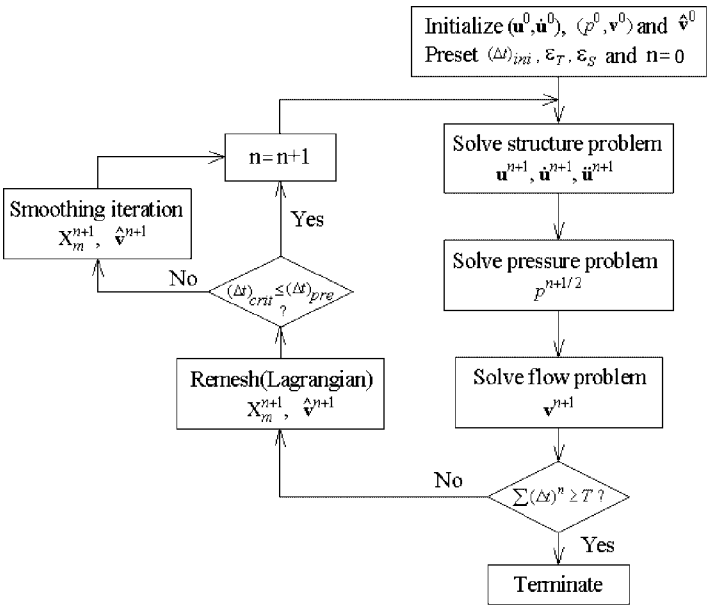

Figure 3. Flowchart for the time-incremental fluid-structure numerical analysis.

appendix). To which we apply the finite element method in order to spatially approximate two step-wise variables. Using isoparametric basis functions, we approximate step-wise velocities and pressures

$$\mathbf{v}^n(\mathbf{x}) = \Phi(\mathbf{x})\bar{\mathbf{v}}^n, \quad p^n(\mathbf{x}) = \Psi(\mathbf{x})\bar{\mathbf{p}}^n \tag{29}$$

where Φ is the $(3 \times 3N)$ matrix and Ψ the $(1 \times N)$ matrix composed of N basis functions. Along the detailed derivation given in the appendix, we finally have a set of fully discretized and fully explicit matrix equations for time-step-wise pressures and velocities:

$$\mathbf{H}\bar{\mathbf{p}}^{n+1/2} = -\frac{1}{\Delta t}\mathbf{G}^{\mathrm{T}}\bar{\mathbf{v}}^n - \mathbf{E}\bar{\mathbf{v}}^{n+1/2} + \Theta^{n+1/2} + \mathbf{b}_P \tag{30}$$

$$\frac{1}{\Delta t}\mathbf{F}(\bar{\mathbf{v}}^{n+1} - \bar{\mathbf{v}}^n) + \mathbf{A}\bar{\mathbf{v}}^n - \mathbf{G}\bar{\mathbf{p}}^{n+1/2} + \mathbf{L}\bar{\mathbf{v}}^{n+1/2} + \frac{\Delta t}{2}(\mathbf{Q}\bar{\mathbf{v}}^{n+1/2} + \mathbf{R}\bar{\mathbf{p}}^{n+1/2} - \mathbf{S}) = \Gamma^{n+1/2} + \mathbf{b}_V \tag{31}$$

As is well presented in Figure 3 showing the flowchart of the time-incremental structure-liquid coupled numerical procedure for our analysis, we first solve Equation (30) for $p^{n+1/2}$ with the predetermined values $\ddot{\mathbf{u}}^n, \ddot{\mathbf{u}}^{n+1}, \mathbf{v}^{n-1}, \mathbf{v}^n, \hat{\mathbf{v}}^n$ and boundary data. Substituting this into Equation (31), together with other predetermined values, provides us $\mathbf{v}^{n+1}$. We emphasis that the mesh velocity $\hat{\mathbf{v}}^n$ is determined *a priori* according to the remeshing scheme described in the next section.

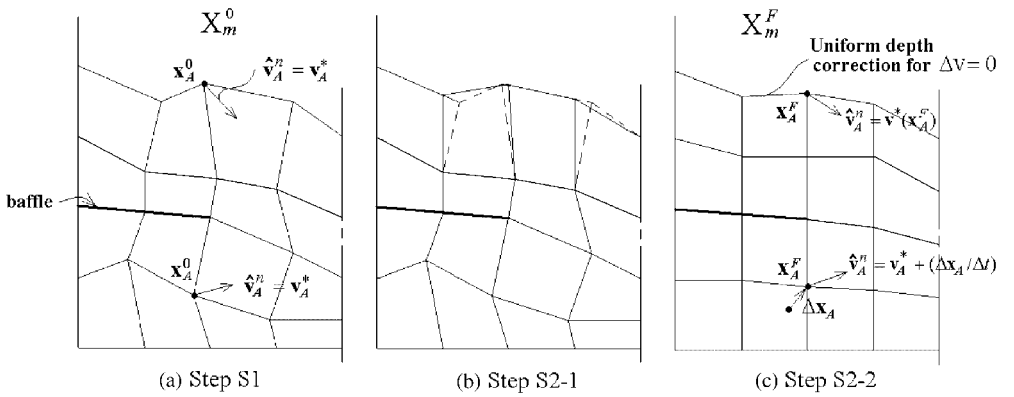

Figure 4. A remeshing procedure composed of three steps (2D illustration).

3.2. *Remeshing in the ALE method*

Regardless of the term *arbitrary*, the mesh velocity $\hat{\mathbf{v}}$ should be chosen from a physical and numerical point of view: (i) it should satisfy

$$(\mathbf{v}^* - \hat{\mathbf{v}}^n) \cdot \mathbf{n} = 0 \quad \text{on } \partial\Omega_F \tag{32a}$$

$$\nabla \cdot (\mathbf{v}^* - \hat{\mathbf{v}}^n) = 0 \quad \text{in } \Omega_F \tag{32b}$$

and (ii) it should not lead any numerical instability owing to the excessive mesh distortion. Hence, its determination becomes a crucial issue in the ALE numerical approach. We note here that the above conditions are identically satisfied in the Lagrangian approach and the latter condition (32b) implies no change in the total liquid volume after the remeshing. So far, several useful remeshing algorithms have been introduced, as is addressed in Reference [15], but the choice of a suitable remeshing scheme depends on the type of problems and numerical schemes for solving Navier–Stokes equations. Usually, the choice is made by combining two or three existing algorithms.

In the current study, the remeshing is performed basically through three steps, as illustrated in Figure 4: (S1) take $\hat{\mathbf{v}}^n = \mathbf{v}^*$ for the whole nodes, and next (S2) smooth the relocated mesh if required, by enforcing the physical requirement (i). Here, the second step is carried out iteratively and split into two steps again: (S2-1) smooth the boundary nodes first and then (S2-2) smooth the interior nodes, in order to minimize the total CPU time required for the smoothing process. The two physical conditions (32a) and (32b) are fulfilled in step (S2-1).

When we denote $\mathbf{x}_A^c$ be the current location of free-surface node A before remeshing, its new location $\mathbf{x}_A^0$ after step (S1) will be

$$\mathbf{x}_A^0 = \mathbf{x}_A^c + \hat{\mathbf{v}}_A^n \Delta t \tag{33}$$

with the mesh velocity $\mathbf{v}_A^0 = \hat{\mathbf{v}}_A^n$. Updating all free-surface nodes generates a new mesh X_m^0 depicted in Figure 4(a). We next decide whether the smoothing is necessary or not, according to the decision criterion described later, and we perform the iterative smoothing procedure if

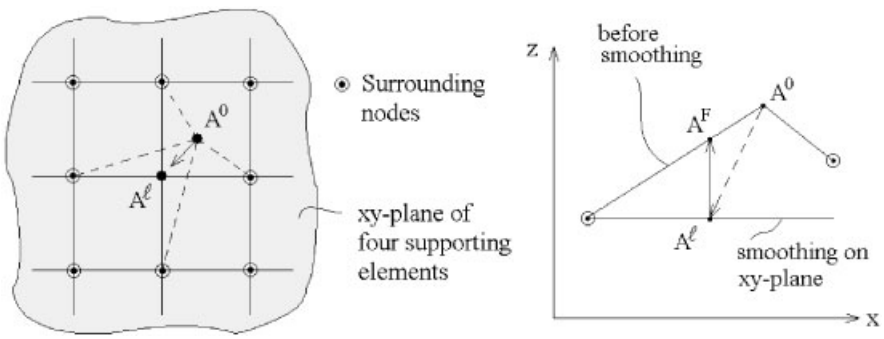

Figure 5. Simple geometric averaging of the boundary nodes.

necessary. For our study, we employ the simple averaging method [15] in which the location of node A is smoothed by averaging the geometric locations of m_A surrounding nodes.

Referring to Figure 5, the surrounding nodes of a boundary node A are composed of the boundary nodes of the elements supporting node A. The free-surface co-ordinates $\mathbf{x}^0$ and mesh velocities $\mathbf{v}^0$ of all supporting elements can be mapped into a 2D bilinear master element. We first smooth two tangential co-ordinate components (on the xy-plane) of node A using the iterative simple averaging method:

$$(x_\alpha)_A^\ell = (x_\alpha)_A^{\ell-1} + \frac{1}{m_A}\sum_{M=1}^{m_A}(x_\alpha)_M, \quad \alpha = t_1, t_2 \text{ and } \ell = 1,2,3,\ldots \tag{34}$$

where (and hereafter) ℓ refers to the iteration cycle. While its normal component $(x_n)_A$ is determined from the basic parametric relation of co-ordinate mapping function. Then, we obtain the final location $\mathbf{x}_A^{\mathrm{F}}$ of boundary node A to be moved and the corresponding mesh velocity $\hat{\mathbf{v}}_A^n = \mathbf{v}^0(\mathbf{x}_A^{\mathrm{F}})$ from the velocity mapping function.

On the other hand, the surrounding nodes of any interior node A are all nodes (except for the node A itself) of the elements supporting the node A. Then, the location of node A is updated through

$$\mathbf{x}_A^\ell = \mathbf{x}_A^{\ell-1} + \frac{1}{m_A}\sum_{M=1}^{m_A}\mathbf{x}_M, \quad \ell = 1,2,3,\ldots \tag{35}$$

Then, the final location of interior node A to be moved is $\mathbf{x}_A^{\mathrm{F}} = \mathbf{x}_A^\ell$ with its final velocity $\hat{\mathbf{v}}_A^n = \mathbf{v}_A^0 + (\mathbf{x}_A^F - \mathbf{x}_A^c)/\Delta t$. After we smooth all of surface and interior nodes, we calculate the total liquid volume of the mesh and compare the initial fuel volume to calculate the volume change ΔV. In order to avoid the volume change accumulation along the time incremental process, we correct the vertical co-ordinates of all free-surface nodes according to

$$(x_n)_A^{\mathrm{F}} = (x_n)_A^{\mathrm{F}} - \Delta V/\mathrm{Area}(\partial\Omega_{\mathrm{F}}^{\mathrm{S}}) \tag{36}$$

This completes the remeshing step to obtain the final mesh X_m^{F} with the updated nodal co-ordinates $\mathbf{x}_A^{\mathrm{F}}$ and the mesh velocity $\hat{\mathbf{v}}^n$, as depicted in Figure 4(c), which is required for the next-step ALE computation.

3.3. Numerical stability and convergence

According to Newmark [20], the constant-averaged-acceleration implicit scheme (19) provides the unconditionally stable time-history response, so the critical time-step for the stable and convergent fluid-structure analysis is decided by the explicit time integration scheme for the fluid response. As is widely known, the convergence and stability of the explicit scheme for Navier–Stokes equations is assured only when the numerical parameters satisfy the Courant criterion:

$$(\Delta t)_{\text{crit}} \leqslant h/(c+u) \tag{37}$$

In which c is the speed of sound in fuel flow, u the flow velocity, and h the smallest distance between two adjacent mesh nodes. It is natural for the analyst to smooth the distorted mesh, in order to suppress the CPU time increase resulted from the critical time-step decrease. However, the implementation of smoothing process at every time stage is not a good idea, because it requires a large number of numerical iterations, as is described in the previous section. Hence, in our study we carry out the smoothing process only when $(\Delta t)_{\text{crit}} \leqslant (\Delta t)_{\text{pre}}$. Here, the preset allowable time-step size $(\Delta t)_{\text{pre}}$ is chosen such that

$$(\Delta t)_{\text{pre}} = \varepsilon_T \cdot (\Delta t)_{\text{ini}} \tag{38}$$

where $(\Delta t)_{\text{ini}}$ refers to the critical time-step size evaluated with the initial mesh.

On the other hand, we should define the time-effective stop criterion for the iterative smoothing process. As can be realized from the previous section, the smoothing process is being performed node-by-node, so it becomes a node-non-linear problem. In the current study, we use the convergence criterion defined by

$$\max_{A \in X_m} |d_A^{\ell+1}|/|d_A^{\ell}| \leqslant \varepsilon_S, \quad \ell = 1, 2, 3, \ldots \tag{39}$$

where $d_A^{\ell} = |\mathbf{x}_A^{\ell} - \mathbf{x}_A^{\ell-1}|$.

4. PARAMETRIC NUMERICAL EXPERIMENTS

In order to examine the effect of baffle on the dynamic response of cylindrical fuel-storage tanks boosting with uniform vertical acceleration, we carried out the parametric numerical experiments by varying the number, the location and the inner-hole diameter of baffle. Numerical simulation was carried out by a test program developed according to the numerical formulations, for which MSC/Patran was incorporated for pre- and post-processing. In Table I, we record the numerical data taken for our numerical experiments. In order to examine the dynamic damping effects of baffle itself we exclude the damping of structure.

Figure 6(a) shows a model tank with two baffles, together with important geometry parameters, where two circumferential edges of top and bottom plates are fixed actually to the main structure of moving vehicle. To which we apply the uniform vertical acceleration of $10g$, and which is numerically implemented by specifying the time-stage-wise displacement boundary conditions. Figures 6(b) and 6(c) represent finite element meshes of structure and fuel, respectively, for which 1800 shell elements and 10 002 three-dimensional trilinear solid elements are used. Even though total element numbers of structure and fuel meshes vary

Table I. Geometry and material data.

	Material data		Geometry data (m)	
Structure	Density ρ_S (kg/m^3)	2.78×10^3	Diameter of tank D	0.4
	Young's modulus E (N/m^2)	7.24×10^{10}	Height of tank H	1.0
	Poisson's ratio v	0.33	Structure thickness t	0.0025
	Yield strength σ_Y (N/m^2)	4.85×10^3	Baffle thickness t_B	0.003
Fuel	Density ρ_F (kg/m^3)	8.15×10^2	Fuel fill height H_F	0.9
	Bulk modulus κ (N/m^3)	2.2×10^9	Inner-hole size D_B	Variable
	Kinematic viscosity μ (Kg/m s)	8.15×10^{-4}	Baffle location H_B	Variable

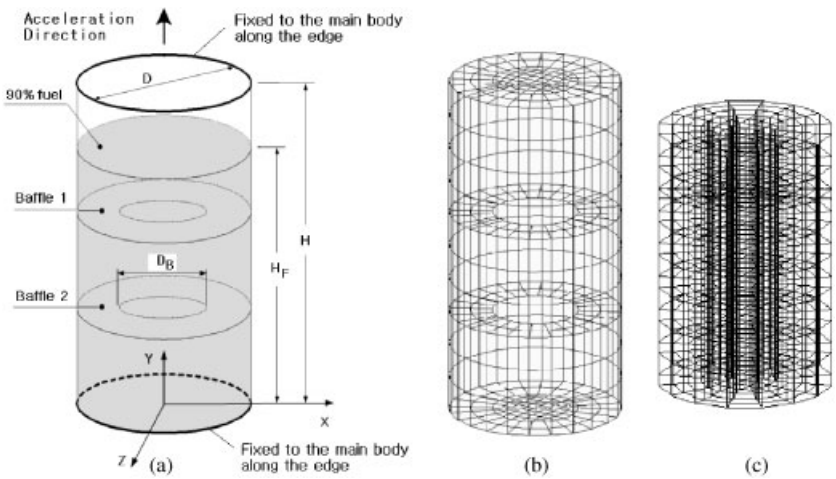

Figure 6. Model tank with two baffles: (a) geometry dimensions; (b) finite element mesh of the structure and; (c) finite element mesh of the interior fuel region.

according to the choice of baffle parameters, the relative change in total element number is not significant.

From the fact that a fuel-storage container accelerating abruptly experiences the severe dynamic loading within an initial short time interval, we take the numerical observation time T by 60 ms. On the other hand, the speed of sound c in fuel is found to be 1640 m/s from the fuel density and the bulk modulus given in Table I. According to the elementary dynamics, we also found that the peak flow velocity does not exceed 10 m/s within the observation time period. Then, according to the Courant criterion (37) the initial fluid mesh shown in Figure 6(c) requires the critical time-step size $(\Delta t)_{\text{crit}}$ of 4.39×10^{-6} s. Referring to Equation (38), we preset ε_T by 0.4 so that the minimum allowable time-step size $(\Delta t)_{\text{pre}}$ becomes to be 1.756×10^{-6} s. For all simulation cases in this study, we choose two simulation parameters ε_T and ε_S by 0.4 and 0.1, respectively. It is worthy noting that the smoothing scheme described in Section 3.2 exhibits rapid convergence speed so that the smoothing process satisfying the preset tolerance is completed in a few iterations.

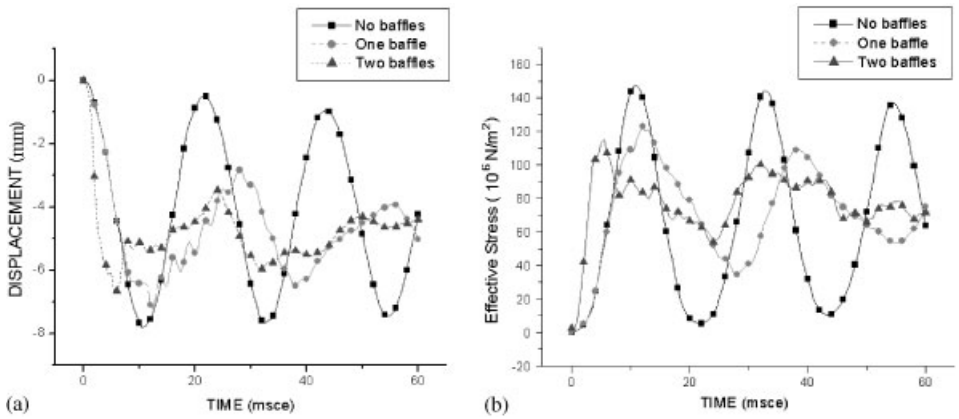

Figure 7. Time-history response of the bottom centre: (a) the relative displacement; and (b) the effective stress.

4.1. *Cases with and without baffle*

We first examine the effect of baffle existence on the structural dynamic response. Referring to Figure 6(a), baffles of the relative inner-hole size $D_B/D = 0.5$ and the uniform spacing are installed. When the fuel-storage tank is subjected to the abrupt acceleration, major portion of the resulting hydrodynamic pressure is acting upon the bottom plate and baffles. Hence, we focus on the dynamic response of these two substructures. Time-history responses of the relative displacement and the effective stress at the bottom centre are represented in Figures 7(a) and 7(b), respectively. Here, the term *relative* indicates the displacement subtracted the rigid-body motion of tank, and hereafter the displacements in plots are in the relative sense.

From two figures, we first see that baffled cases produce much lower displacements and effective stresses than the no-baffle case. Needless to say, it is because baffles are taking care of certain amount of hydrodynamic pressure force. In addition, the time-history response of baffled cases becomes stabilized much faster, while exhibiting higher response frequency, so that the dynamic damping effect of baffle is clearly confirmed. As will be given later, the flow pattern becomes more complex as the baffle number increases, and which makes the response frequency be lower. Even though the two-baffle case produces smaller displacement and effective stress than the one-baffle case, the dynamic damping effect is not shown to be proportional to the baffle number. The detailed numerical results showing the variation of dynamic damping effects to the baffle number will be provided in the next section.

Figure 8 shows distributions of the effective stress occurred at the bottom plate, for three cases, when the effective stress reaches maximum and minimum. Clearly, the peak value decreases in proportional to the baffle number. But, the minimum value increases remarkably with the baffle number increase, and which confirms that the time-history response of effective stress becomes steadier as the baffle number increases. Hydrodynamic pressure distributions of three cases at the time when the effective stress reaches maximum and minimum are given in Figure 9. Where we observe that the maximum and minimum pressures increase monotonically as the baffle number increases. Needless to say, it is because the flow field becomes more

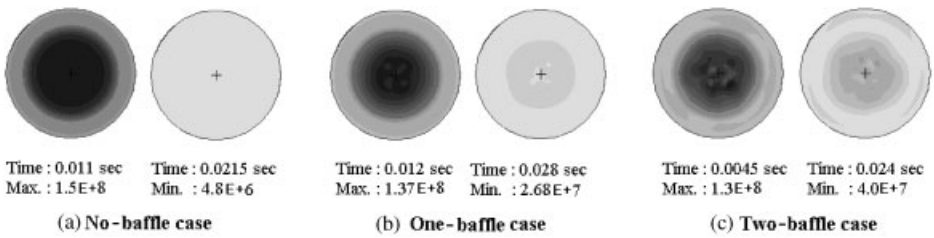

Figure 8. Effective stress distributions when it reaches maximum and minimum: (a) no baffle; (b) one baffle; and (c) two baffles (unit: N/m^2).

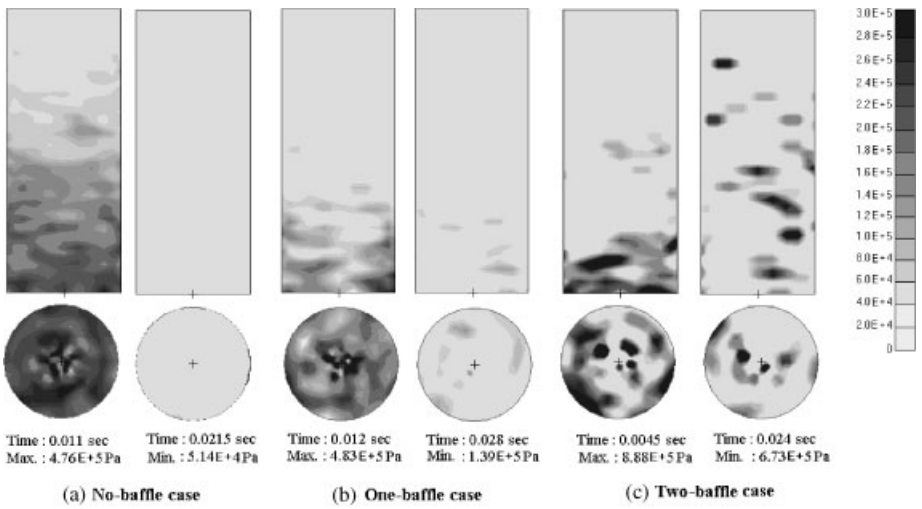

Figure 9. Hydrodynamic pressure distributions when the effective stress reaches maximum and minimum: (a) no baffle; (b) one baffle; and (c) two baffles.

complex in proportional to the baffle number, and which produces higher gradient in the flow velocity field.

Flow patterns of interior fuel in the no-baffle and two-baffle cases are shown in Figures 10 and 11. When the baffle is not inserted, flow field is simple showing clear directional characteristics and almost uniform at each time stage, but it becomes very complex and non-uniform with the time stage when baffles are inserted. Furthermore, we can see the vortex flows within compartmented subregions, as well as the main flow through baffle inner-holes and the oscillatory motion of baffles. In addition, the flow velocity shows remarkable decrease in its magnitude with time, Considering all these dynamic characteristics, we can recognize the substantial dynamic damping effect of baffles on the flow motion.

For one- and two-baffle cases, we plot time-history responses of the relative displacement at the baffle free-edge. Compared to those shown in Figure 7(a) at the bottom plate, the baffle response is more oscillatory with higher frequencies. But, the peak displacements are less than that of the bottom centre, and which indicates baffles sustain less hydrodynamic pressure force

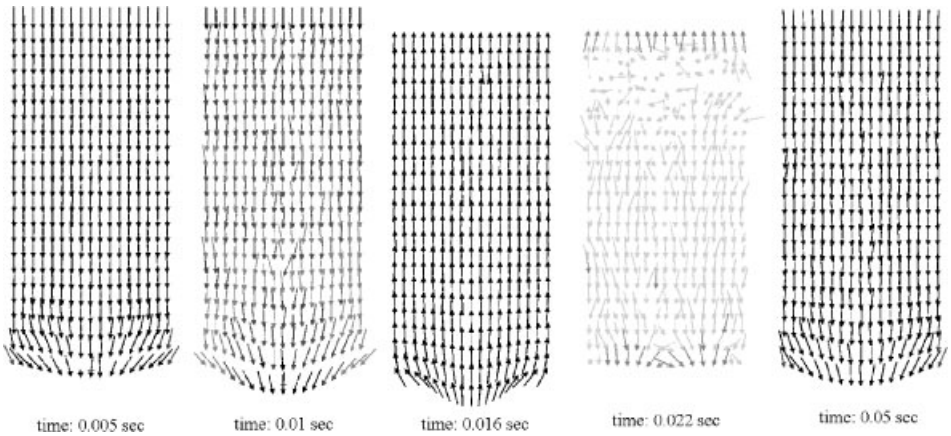

Figure 10. Internal flow profiles at five different time stages (no baffle).

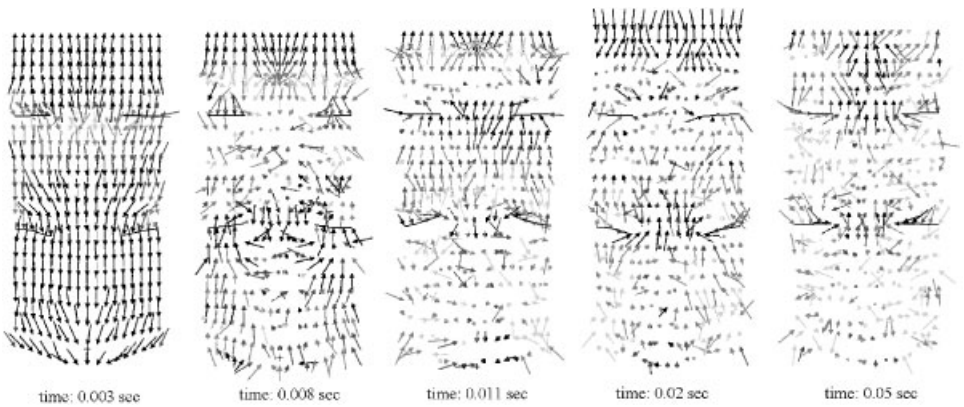

Figure 11. Internal flow profiles at five different time stages (two baffles).

than the bottom plate. On the other hand, the one-baffle case produces larger displacement with lower response frequency than the two-baffle case. When restricted to the two-baffle case, the lower baffle produces larger displacement than the upper one at the beginning, but the difference in magnitude between lower and upper baffles becomes insignificant with the time increase.

Figure 12(b) comparatively represents time-history responses of the effective stress occurred at the 1/3 point of baffle width from the free-edge, where the remarkable stress reduction is observed when two baffles are installed. While the effective stress at the bottom centre does not drop remarkably when one baffle is substituted with two baffles, when compared with Figure 7(b). Hence, from the stress-magnitude point of view, we realize that the response of baffle is sensitive to the baffle number but that of the bottom centre is not. Further parametric investigation of the baffle effects on the dynamic response to the baffle location and inner-hole diameter as well as the baffle number will be intensively described in the next

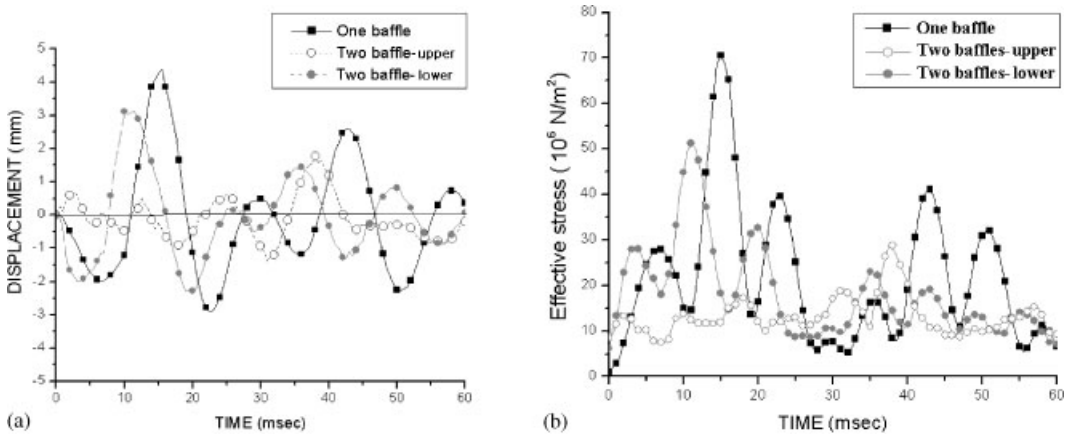

Figure 12. Time-history responses of baffle: (a) the relative free-edge displacement; and (b) the effective stress.

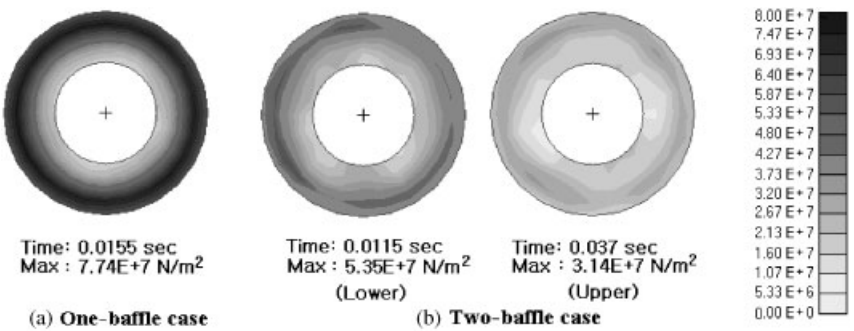

Figure 13. Effective stress distributions of baffles when it reaches maximum: (a) one-baffle case; and (b) two-baffle case.

section. Figure 13 shows the effective stress distributions when each baffle reaches the peak value.

4.2. *Parametric baffle effects*

In order for more comprehensive understanding of the dynamic damping effects of baffle, we in this section intend to examine sort of asymptotic dynamic characteristics to the baffle number. As well, we consider a various combinations of the baffle location H_L and inner-hole diameter D_B by restricting to the one-baffle case. The dynamic damping effect is estimated based on four measurements: the maximum displacement and effective stress, the response frequency (Hz) and the logarithmic decrement ς_d defined by

$$\varsigma_d = \frac{\ln |u_p^1/u_p^N|}{N} \tag{40}$$

Table II. Parametric dynamic response of the bottom centre to the baffle number ($D_B/D = 0.5$).

Item	Baffle number					
	0	1	2	3	4	5
Max. displacement (mm)	7.81	7.21	6.65	7.07	7.18	7.30
Max. effective stress (MPa)	151.2	137.5	129.3	133.9	137.9	141.9
Response frequency (Hz)	45.9	38.5	33.9	30.1	31.5	32.4
Logarithmic decrement ($\times 10^{-2}$)	2.4	6.7	7.1	9.5	10.4	12.2

Table III. Parametric results on the peak displacement (and the maximum effective stress) of baffles ($D_B/D = 0.5$, unit: mm and MPa).

	Baffle number				
	1	2	3	4	5
First from the free-surface	4.37 (77.4)	1.81 (31.4)	2.09 (34.6)	3.04 (52.0)	2.67 (44.2)
Second		3.12 (53.5)	2.12 (34.5)	1.53 (22.6)	1.40 (20.2)
Third			2.30 (38.6)	1.63 (24.2)	1.41 (20.7)
Fourth				1.65 (27.5)	1.43 (21.1)
Fifth					1.42 (21.0)

In which u_p^1 and u_p^N denote the first peak and the next available Nth peak in the displacement time-history response. The response frequency is to estimate the stabilization tendency of the transient dynamic response, that is, the response becomes more stabilized as it becomes smaller. While, the third estimate is for measuring the damping intensity such that the response decays more quickly as it becomes larger.

As recorded in Table II we measured four quantities at the centre of bottom plate by increasing the baffle number. We note that same baffles with D_B/D of 0.5 are installed with uniform spacing in the axial direction, so the baffle locations are changed according to the baffle number. The logarithmic decrement shows a monotonic improvement to the baffle number. The other quantities display a continuous improvement, up to a certain baffle number, but become worse after that. Referring to Figures 7(a) and 7(b), together with the monotonic improvement in the logarithmic decrement, this peculiar variation implies that the dynamic damping effect does not improve successively with the simple increase of the number of baffles spaced uniformly, particularly at the initial stage. Meanwhile, we record maximum displacements and effective stresses occurred at individual baffles in Table III. The maximum displacement and effective stress, except for the top baffle exhibiting the remarkable fluctuation variation, decrease uniformly in proportional to the baffle number increase. We observe that the top baffle is significantly influenced by its vertical location. Furthermore, the lowest baffle experiences the largest deformation and effective stress until the three-baffle case, but the top baffle do after that. So, we can infer that these phenomena cause the above-mentioned peculiar variation at the bottom plate. From this point of view, we need to investigate the parametric dynamic damping characteristics to other design parameters, such as the baffle location and the inner-hole diameter.

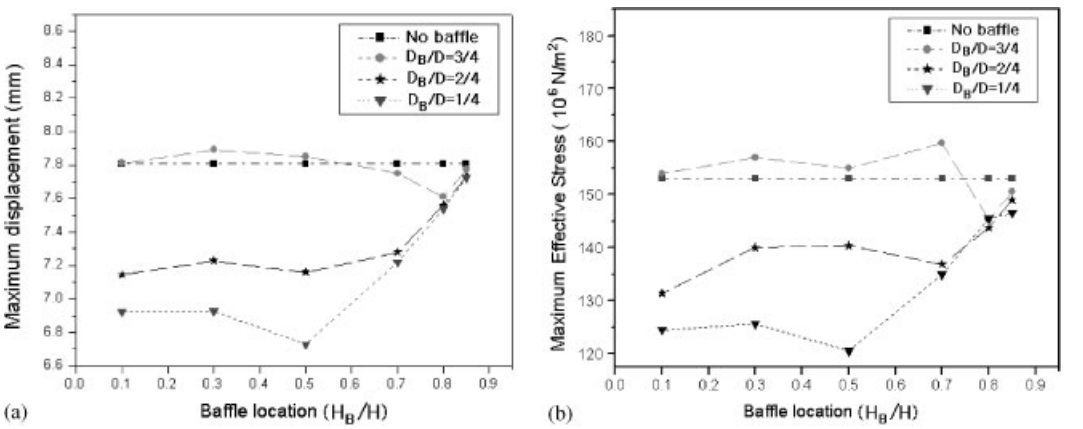

Figure 14. Parametric dynamic response of the bottom centre to the baffle location and inner-hole diameter: (a) maximum displacement; and (b) maximum effective stress.

We next examine the parametric damping effects of baffle with respect to the baffle location and inner-hole diameter. For this purpose, we consider six baffle locations $H_L/H = 0.1$, 0.3, 0.5, 0.7, 0.8 and 0.85 and three inner-hole diameters $D_B/D = \frac{1}{4}, \frac{2}{4}$ and $\frac{3}{4}$, in the one-baffle case.

The maximum displacement and effective stress decrease in proportion to the decrease of D_B/D, as shown in Figures 14(a) and (b), but this dependence on the baffle inner-hole size approaches the no-baffle case as the baffle approaches the fuel free surface. In particular, the inner-hole size $D_B/D = \frac{3}{4}$ for certain baffle locations produces the response worse than the no-baffle case. Needless to say, it is because the hydrodynamic force acting on the bottom plate becomes smaller as the inner-hole size decreases due to more suppression of fuel flow. However, the flow suppression becomes negligible as the baffle approaches the fuel free surface. The variation of maximum displacement and effective stress to the baffle location $H_B/H \leqslant 0.5$ is not shown remarkable, when compared to the variation to the inner-hole size. The lowest case in the maximum displacement and effective stress is when $D_B/D = \frac{1}{4}$ and $H_B/H = 0.5$. So, the baffle effect reduces either the baffle location approaches the free surface or the baffle inner-hole size becomes larger.

Figures 15(a) and 15(b) show the variation of the peak displacement and maximum effective stress occurred at the baffle, respectively. When compared with Figures 14(a) and 14(b), the baffle exhibits the almost contrary parametric behaviour. It is because the more hydrodynamic force the baffle supports the less the bottom plate does and vice versa. Hence, this mutually conflicting characteristic should be reflected in the design of baffled fuel-container.

Figure 16(a) represents the response-frequency variation of the displacement time-history response of the bottom centre. Examining with respect to the baffle inner-hole size, the case of $D_B/D = \frac{1}{4}$ exhibits the highest frequency while the case with $D_B/D = \frac{2}{4}$ does the lowest one, but this distinction disappears when the baffle location approaches the fuel free surface. This can be explained as follows. Until the critical value of D_B/D, the decrease of baffle inner-hole size continuously delays the major fluid flow, but further decrease beyond the critical value separates the major fluid flow into the compartmented flow regions, as shown in Figure 11. In

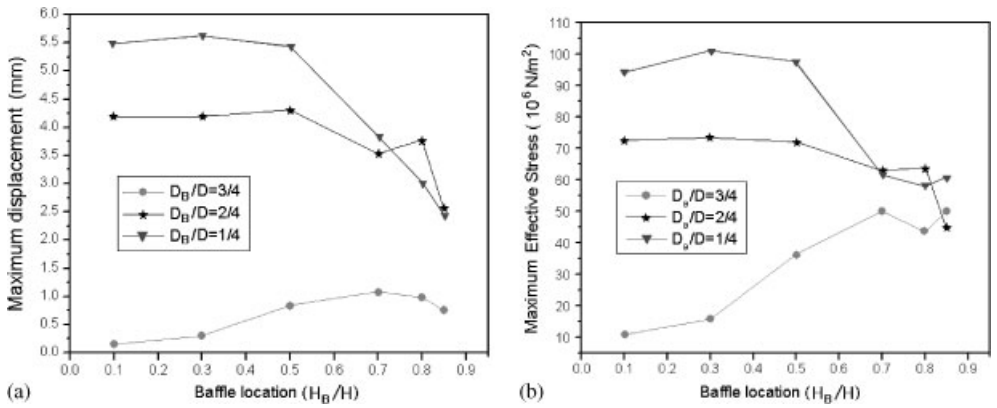

Figure 15. Parametric dynamic response of baffle to the baffle location and inner-hole diameter: (a) maximum displacement; and (b) maximum effective stress.

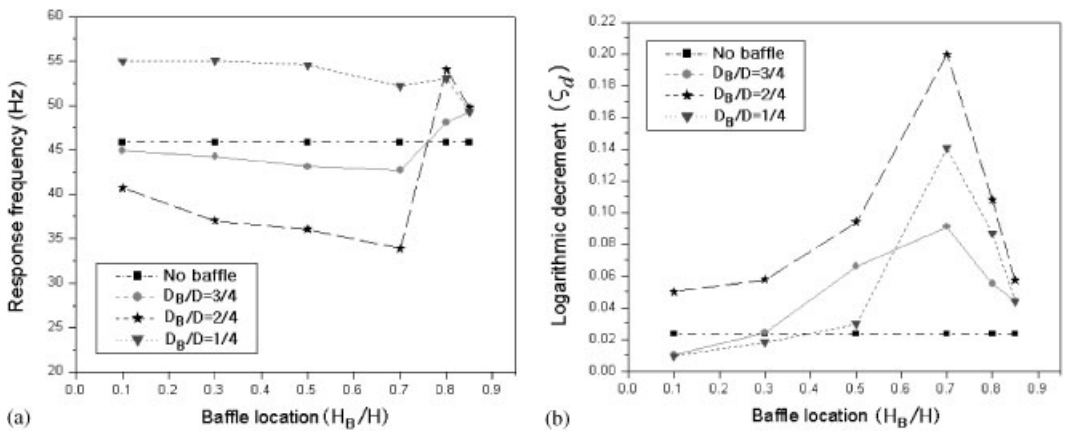

Figure 16. Parametric dynamic damping effect to the baffle location and inner-hole diameter: (a) response frequency; and (b) logarithmic decrement.

general, the compartmented liquid container exhibits higher response frequency compared to non-compartmented one [21]. Even though slightly, the response frequency decreases as the baffle location goes up until $H_B/H \leqslant 0.7$, but it remarkably increases to the same limit when $H_B/H > 0.7$. Hence, one should determine the inner-hole size by combining this tendency with the previous result that the baffle location should not be too high or too low.

The variation of logarithmic decrement is represented in Figure 15(b), where we confirm that almost all cases have higher decrements than the no-baffle case. Regardless of the baffle inner-hole diameter, the logarithmic decrement increases with the baffle location until $H_B/H = 0.7$, but it strictly drops to the no-baffle case when $H_B/H > 0.7$. In the same manner, the baffle inner-hole diameter D_B/D of $\frac{2}{4}$ produces the best logarithmic decrement.

5. CONCLUSIONS

This paper addressed the parametric investigation on the dynamic damping effects of disc-type baffle, for cylindrical fuel-storage container in an abrupt boosting motion, by the coupled time-incremental finite element method. The structural dynamic response is solved by the unconditionally stable and convergent Newmark method while the internal fuel flow by the accurate C-fractional method in the ALE kinematic description. As well, we used the selective mesh-smoothing scheme in order for the time-effective numerical implementation, as well as fairly regular meshes during the entire analysis interval by presetting the minimum allowable time-step size. Through numerical experiments, we confirmed that the coupled ALE finite element method used in this study successfully and effectively performs the dynamic analysis of baffled fuel-storage containers.

By varying the number, the installation location and the inner-hole diameter of baffle, we parametrically investigated the variation of baffle damping effects with respect to four major dynamic characteristics. According to the numerical results the following main observations and suggestions are drawn.

1. The dynamic response of the bottom plate is not continuously improved in proportional to the number of baffles with uniform installation spacing. Meanwhile, the peak dynamic response of baffle decreases monotonically with the baffle number increase, except for the top one exhibiting the remarkable fluctuating response to its vertical location.
2. The damping effect deteriorates either when the baffle location is too high or too low, or when the inner-hole diameter is too wide or too narrow. On the other hand, the baffle and the bottom plate display the mutually contrary parametric variations, with respect to these two parameters. Thus, both parameters should be appropriately selected for the desired dynamic damping effect.
3. In our simulation model, the best damping effect is achieved when the inner-hole diameter D_B is $0.5D$ and the top baffle is located at 65–75% of the fill height of fuel.

APPENDIX A: MATRIX EQUATIONS FOR PRESSURE AND VELOCITY

In order for the mathematical expression convenience, we adopt here the vector notation. The variational formulation of the time-step-wise velocity Equation (25) becomes as follows: For every virtual velocity $\mathbf{w}$ with $\mathbf{v}^n$ and $p^{n+1/2}$, find $\mathbf{v}^{n+1}$ such that

$$\frac{1}{\Delta t}\int_{\Omega_F}\mathbf{w}\cdot(\mathbf{v}^{n+1}-\mathbf{v}^n)\,dV+\int_{\Omega_F}\mathbf{w}\cdot[(\mathbf{v}^*-\hat{\mathbf{v}}^n)\cdot\nabla]\mathbf{v}^n\,dV-\int_{\Omega_F}(\nabla\cdot w)p^{n+1/2}\,dV$$
$$+\int_{\Omega_F}\frac{\mu}{\rho_F}\nabla\mathbf{w}:\nabla\mathbf{v}^{n+1/2}\,dV+\frac{\Delta t}{2}\int_{\Omega_F}\Lambda^{n+1/2}\cdot[(\mathbf{v}^*-\hat{\mathbf{v}}^n)\cdot\nabla]\mathbf{w}\,dV$$
$$=\int_{\partial\Omega_F^S}\hat{\mathbf{t}}^{n+1/2}\cdot\mathbf{w}\,ds+\int_{\Omega_F}\mathbf{w}\cdot\mathbf{g}\,dV \tag{A1}$$

with

$$\Lambda^{n+1/2} = [(\mathbf{v}^* - \hat{\mathbf{v}}^n) \cdot \nabla]\mathbf{v}^{n+1/2} + \frac{1}{\rho_F} \nabla p^{n+1/2} - \frac{\mu}{\rho_F} \Delta \mathbf{v}^{n+1/2} - \mathbf{g} \tag{A2}$$

During the above integration by parts, the next conditions that will be used for the mesh smoothing are enforced for all time steps:

$$\nabla \cdot (\mathbf{v}^* - \hat{\mathbf{v}}^n) = 0 \quad \text{in } \Omega_F \tag{A3}$$

$$(\mathbf{v}^* - \hat{\mathbf{v}}^*) \cdot \mathbf{n} = 0 \quad \text{on } \partial\Omega_F \tag{A4}$$

We note that the third term in Equation (A2) vanishes in low-order finite elements.

By defining the divergence-like operator $\mathbf{D}$ by $\{\partial/\partial x, \partial/\partial y, \partial/\partial z\}^T$, together with Equation (28), we can easily derive

$$(\mathbf{s} \cdot \nabla)\mathbf{v} = (\bar{\mathbf{s}}^{n^T} \mathbf{B}^T \mathbf{I})\Phi\bar{\mathbf{v}}, \quad \mathbf{B} = \mathbf{D}^T\Phi \tag{A5}$$

In which, $\mathbf{I}$ denotes the (3×3) identity matrix, and $\bar{\mathbf{s}}^n$ the step-wise nodal vector of the convection velocity $(\mathbf{v}^* - \hat{\mathbf{v}}^n)$. Introducing the isoparametric approximation (29) into the variational form, we have

$$\begin{aligned}
&\mathbf{F} = \int_{\Omega_F} \Phi^T\Phi \, dV, \quad \mathbf{A} = \int_{\Omega_F} \Phi^T(\bar{\mathbf{s}}^{n^T}\mathbf{B}^T\mathbf{I})\Phi \, dV, \quad \mathbf{G} = \int_{\Omega_F} \mathbf{B}^T\Psi \, dV \\
&\mathbf{L} = \int_{\Omega_F} \frac{\mu}{\rho_F} \tilde{\mathbf{B}}^T\tilde{\mathbf{B}} \, dV, \quad \mathbf{Q} = \int_{\Omega_F} \Phi^T(\bar{\mathbf{s}}^{n^T}\mathbf{B}^T\mathbf{I})^T(\bar{\mathbf{s}}^{n^T}\mathbf{B}^T\mathbf{I})\Phi \, dV \\
&\mathbf{R} = \int_{\Omega_F} \Phi^T(\bar{\mathbf{s}}^{n^T}\mathbf{B}^T\mathbf{I})^T\nabla\Psi \, dV, \quad \mathbf{S} = \int_{\Omega_F} \Phi^T(\bar{\mathbf{s}}^{n^T}\mathbf{B}^T\mathbf{I})^T\mathbf{g} \, dV \\
&\mathbf{b}_V = \int_{\Omega_F} \Phi^T\mathbf{g} \, dV, \quad \Gamma = \int_{\Omega_F} \Phi^T\hat{\mathbf{t}}^{n+1/2} \, ds
\end{aligned} \tag{A6}$$

with $\tilde{\mathbf{B}} = \tilde{\mathbf{D}}^T\Phi$. In which, $\tilde{\mathbf{D}}^T$ refers to the (9×3) differential operator defining the (9×1) vector of $\nabla\mathbf{v}$. With the matrices defined above, we can express the resulting finite element equations as follows:

$$\begin{aligned}
&\frac{1}{\Delta t}\mathbf{F}(\bar{\mathbf{v}}^{n+1} - \bar{\mathbf{v}}^n) + \mathbf{A}\bar{\mathbf{v}}^n - \mathbf{G}\bar{\mathbf{p}}^{n+1/2} + \mathbf{L}\bar{\mathbf{v}}^{n+1/2} + \frac{\Delta t}{2}(\mathbf{Q}\bar{\mathbf{v}}^{n+1/2} + \mathbf{R}\bar{\mathbf{p}}^{n+1/2} - \mathbf{S}) \\
&= \Gamma^{n+1/2} + \mathbf{b}_V
\end{aligned} \tag{A7}$$

Along the similar procedure, we can derive the Galerkin formulation of the time-step-wise pressure Equation (27): With the values determined at previous step, find $p^{n+1/2}$ such that

$$\int_{\Omega_F} \frac{1}{\rho_F} \nabla p^{n+1/2} \cdot \nabla q \, dV = -\frac{1}{\Delta t} \int_{\Omega_F} (\nabla \cdot \mathbf{v}^n) q \, dV - \int_{\Omega_F} \nabla q \cdot [(\mathbf{v}^* - \hat{\mathbf{v}}^n) \cdot \nabla] \mathbf{v}^{n+1/2} \, dV + \int_{\Omega_F} \frac{\mu}{\rho_F} \nabla q \cdot \Delta \mathbf{v}^{n+1/2} \, dV + \int_{\Omega_F} \nabla q \cdot \mathbf{g} \, dV + \int_{\partial\Omega_I} \gamma^{n+1/2} q \, dV \tag{A8}$$

for every virtual pressure q. For which we apply the integration by parts to the terms $[\cdot]$ in Equation (27). We introduce the finite element approximation (29) and define the following coefficient matrices given by

$$\mathbf{H} = \int_{\Omega_F} \frac{1}{\rho_F} (\nabla \Psi)^T \nabla \Psi \, dV, \quad \mathbf{E} = \int_{\Omega_F} (\nabla \Psi)^T (\bar{\mathbf{s}}^{n^T} \mathbf{B}^T \mathbf{I}) \Phi \, dV$$
$$\mathbf{b}_P = \int_{\Omega_F} (\nabla \Psi)^T \mathbf{g} \, dV, \quad \Theta^{n+1/2} = \int_{\partial\Omega_I} \Psi^T \gamma^{n+1/2} \, ds \tag{A9}$$

Then, we obtain the system of simultaneous equations given by

$$\mathbf{H} \bar{\mathbf{p}}^{n+1/2} = -\frac{1}{\Delta t} \mathbf{G}^T \bar{\mathbf{v}}^n - \mathbf{E} \bar{\mathbf{v}}^{n+1/2} + \Theta^{n+1/2} + \mathbf{b}_p \tag{A10}$$

ACKNOWLEDGEMENTS

The financial support for this work by Agency for Defense Development under Contract No. ADD-00-5-6 is gratefully acknowledged.

REFERENCES

1. Morand HJP, Ohayon R. *Fluid Structure Interaction: Applied Numerical Methods*. Wiley: New York, 1995.
2. Noji T, Yoshida H, Tatsumi E, Kosaka H, Hagiuda. Study of water-sloshing vibration control damper, Part 1: hydrodynamic force characteristics of the device and damping effect of the system. *Journal of Structural and Construction Engineering* 1990; **411**:97–105.
3. Welt F, Modi VJ. Vibration damping through liquid sloshing, Part 2: experimental results. *Journal of Vibration and Acoustics* 1992; **114**:17–23.
4. Housner GW. Dynamic pressure on accelerated fluid containers. *Bulletin of Seismological. Society of America* 1957; **47**:15–35.
5. Abramson HN. *The Dynamic Behavior of Liquids in Moving Containers*. NASA SP-106, 1966.
6. Bauer HF. Nonlinear mechanical model for the description of propellant sloshing. *AIAA Journal* 1966; **4**(9): 1662–1668.
7. Silveira AM, Stephens DG, Leonard HW. An experimental investigation of liquid oscillations in tanks with various baffles. *NASA Technical Note* D-715, 1961.
8. Hung RJ, Pan HL. Baffle effect on sloshing-modulated torques responsed to orbital accelerations in microgravity. *Journal of Spacecraft and Rockets* 1995; **32**(4):723–731.
9. Zienkiewicz OC, Taylor RL. *The Finite Element Method*, vol. 2. McGraw-Hill: Singapore, 1991.
10. Cho JR, Song JM. Assessment of classical numerical models for the separate liquid-structure analysis. *Journal of Sound and Vibration* 2001; **239**(5):995–1012.

11. Hirt CW, Amsden AA, Cook JL. An arbitrary Lagrangian–Eulerian computing method for all flow speeds. *Journal of Computational Physics* 1974; **14**:227–253.
12. Belytschko T, Kennedy JM. Computer models for subassembly simulation. *Nuclear Engineering Design* 1978; **49**:17–38.
13. Benson DJ. An efficient, accurate, simple ALE method for nonlinear finite element programs. *Computational Methods in Applied Mechanics and Engineering* 1989; **72**:305–350.
14. Oden JT, Demkowicz LF. *Applied Functional Analysis*. CRC Press: New York, 1996.
15. Souli M, Ouahsine A, Lewin L. ALE formulation for fluid-structure interaction problems. *Computational Methods in Applied Mechanics and Engineering* 2000; **190**:659–675.
16. Bathe KJ. *Finite Element Procedures*. Prentice-Hall: Singapore, 1996.
17. Hayashi M, Hatanaka K, Kawahara M. Lagrangian finite element method for free surface Navier–Stokes flow using fractional step methods. *International Journal for Numerical Methods in Fluids* 1991; **13**:805–840.
18. Chorin AJ. Numerical solution of the Navier–Stokes equations. *Mathematics of Computation* 1968; **22**: 745–762.
19. Nonino C, Giudice SD. Finite element analysis of turbulent forced convection in lid-driven rectangular cavities. *International Journal for Numerical Methods in Engineering* 1988; **25**:313–329.
20. Newmark NM. A method of computation for structural dynamics. *ASCE Journal of Engineering Mechanics Division* 1959; **85**:67–94.
21. Abramson HN, Garza LR. Some measurements of the effects of ring baffles in cylindrical tanks. *Journal of Spacecraft Rockets* 1964; **1**(5):560–564.

